Energy Storage Materials 63 (2023) 102927

Contents lists available at ScienceDirect

Energy Storage Materials

journal homepage: www.elsevier.com/locate/ensm

Modeling the 4D discharge of lithium-ion batteries with a multiscale time-dependent deep learning framework

Agnese Marcato [a,b], Javier E. Santos [b,c], Chaoyue Liu [d,e], Gianluca Boccardo [a,**], Daniele Marchisio [a], Alejandro A. Franco [d,e,f,g,*]

[a] Department of Applied Science and Technology, Politecnico di Torino, Corso Duca degli Abruzzi 24, Torino 10129, Italy
[b] Center for Nonlinear Studies, Los Alamos National Laboratory, Los Alamos, NM 87545, USA
[c] Earth and Environmental Science Division, Los Alamos National Laboratory, Los Alamos, NM 87545, USA
[d] Laboratoire de Réactivité et Chimie des Solides (LRCS), Unité Mixte de Recherche CNRS 7314, Université de Picardie Jules Verne, Hub de l'Energie, 15 rue Baudelocque, Amiens 80039, France
[e] Réseau sur le Stockage Electrochimique de l'Energie (RS2E), Fédération de Recherche CNRS 3459, Hub de l'Energie, 15 rue Baudelocque, Amiens 80039, France
[f] ALISTORE-European Research Institute, Fédération de Recherche CNRS 3104, Hub de l'Energie, 15 rue Baudelocque, Amiens 80039, France
[g] Institut Universitaire de France, 103 Boulevard Saint Michel, Paris 75005, France

ARTICLE INFO

Keywords:
Machine learning
Neural networks
Lithium-ion batteries

ABSTRACT

The lithium-ion battery (LIB) field is moving towards the direction of investigating spatially resolved physical phenomena in the 3D porous microstructure of electrodes. These pore-scale simulations give new insights into the local dynamics of lithiation/de-lithiation and charge transport. Nevertheless, the computational time of these simulations limits the integration of these models in optimization workflows of cycling conditions or electrode manufacturing processes.

Machine learning models present a way of assessing in real-time the performance of materials. While several successful techniques for replicating simulations with machine learning have been proposed, this case study presents a more demanding problem, due to the necessity of understanding the behavior of heterogeneous 3D local data, as it evolves in time: this poses both a scientific and a technical challenge.

To this end, we propose an autoregressive multiscale convolutional neural network model to predict relevant quantities at the pore-scale in the solid phase: the lithium concentration (in the active material) and potential (in the active material and carbon binder). These are ultimately used to reconstruct the battery discharge curve. 3D images of the electrode microstructures are the input to the network, trained with a dataset of finite element method simulations to predict the discharge behavior of the cathode side in lithium ion batteries.

We propose this machine learning model as a proof-of-concept of the applicability of multiscale networks for time-dependent physics problems. The trained model exhibits very high accuracy (with errors lower than 2%) in forecasting the discharge behavior of new unseen cathodes.

1. Introduction

The study of lithium transport and charge dynamics in lithium-ion batteries (LIBs) is a research field of the utmost importance for battery development. The computational modeling of charge-discharge dynamics in LIBs is crucial to ensure their optimal usage in terms of safe charging and discharging cycles; beyond their use for the continuous improvement of battery management systems, these models are also essential in effective design of new battery chemistries and materials [1]. Accurate multiscale models can help researchers to understand the effect of operating conditions on the battery performance, as well as the impact of electrode properties, or the physics behind degradation phenomena [2,3]. The main objective is to exploit models and experiments in synergy to speed up the discovery of new batteries and the understanding of the degradation phenomena impacting the life cycle of state-of-the-art batteries [4].

* Corresponding author at: Laboratoire de Réactivité et Chimie des Solides (LRCS), Unité Mixte de Recherche CNRS 7314, Université de Picardie Jules Verne, Hub de l'Energie, 15 rue Baudelocque, Amiens 80039, France.
** Co-corresponding author at: Department of Applied Science and Technology, Politecnico di Torino, Corso Duca degli Abruzzi 24, Torino 10129, Italy.
E-mail addresses: gianluca.boccardo@polito.it (G. Boccardo), alejandro.franco@u-picardie.fr (A.A. Franco).

https://doi.org/10.1016/j.ensm.2023.102927
Received 12 May 2023; Received in revised form 21 July 2023; Accepted 11 August 2023
Available online 17 August 2023

In the last decades, modeling solutions have been proposed to provide researchers with reliable predictions of integral quantities of interest. Pseudo 1D and 2D models [5–7] have been developed for the electrochemical modeling of batteries and can be easily employed since they can be run on conventional consumer-grade computers. Many open-source implementations exist [8], some of them employing the well-known Newman model [9]. Nevertheless, low-dimensionality models rely on integral descriptors of the electrodes geometries (porosity and tortuosity), as their 3D porous structure is not explicitly considered. However, since these porous structures are now becoming available from imaging techniques [4,10] it does make sense to reproduce them *in silico* [11–14] and exploit them in fully-resolved pore-scale simulations. The explicit consideration of these electrode microstructures in electrochemical models is important to understand the effect of manufacturing parameters and heterogeneities in lithiation/de-lithiation on the performance and aging [15]. Lu et al. [10] reported that complex physics interplay was found in different electrode designs. De Lauri et al. [16] investigated the relationship between heat generation and electrode microstructure. Parmananda et al. [17] found that the homogeneity of graphite particle morphology is important to the anode performance. Therefore, the technique shows great potential in further elevating the electrode performance to another level in various perspectives.

Fully-resolved pore-scale models have been developed thanks to the increasing computational resources available nowadays: these 4D models (3D microscale geometry plus time dependency) do not rely on integral geometrical descriptors of the electrodes as inputs, since the charge and transport equations are solved imposing the boundary conditions on the interfaces between the constituting materials and the pores [18–21]. The pore-scale results give an insight into the local dynamics of lithium and charge transport, beyond macroscale predictions which can be experimentally measured and validated. In literature both *in-silico* generated microstructures and digital images have been employed to this end [22]. Pore network modeling has also been employed recently for the simulation of charge/discharge in lithium-ion batteries as well [23]. In general, the insights given by this closer look at the transport processes happening at, and regulated by, the microscopic scale of the electrodes are essential for understanding the links between electrochemistry and transport processes. This better understanding can help at optimizing the electrodes.

Even though these simulations are practicable for small campaigns, their computational cost is a limitation to integrate these models in optimization workflows [24], or as support in manufacturing laboratories as digital twins of the battery electrochemical behavior. As a promising alternative, surrogate models can be trained to learn from datasets of physics-based simulations, and the trained model can be used to predict outputs fast – in the order of seconds – on new (unseen) data. Neural networks are usually the models of choice since they can learn highly nonlinear correlations between inputs and outputs data with ease [3,25–27]. In particular, convolutional neural networks (CNN) have been widely used in porous media research since they are well-suited to work with image data as inputs and outputs. CNNs have been trained for segmentation tasks [28,29], for parameter estimation [30–32], and for field prediction [33,34]. Nevertheless, there is a tradeoff between the size of the input (and output) images and the number of trainable parameters of the network, due to the memory limitations of graphics processing units (GPU).

The multiscale convolutional neural network (MSNet) [35] overcomes this limitation since its parameters are distributed among different resolutions (scales) of the input images resulting in the capability of studying larger images with wider fields of vision. This model has been adapted for the steady-state prediction of flow fields [35], concentration fields [36], and electrical potentials [37,38] in porous media.

We propose a novel autoregressive multiscale network to learn from a transient dataset of physics-based simulations. We focused on obtaining local predictions of lithium concentration and potential in the solid phase (active material in the former and both active material and carbon binder in the latter) in time over a discharge cycle, resulting in discharge curves.

The dataset is generated using 4D finite element simulations of discharge in the cathode side (half-cell simulations) of LIB cells. The microscale simulations are solved by a finite element method employing in silico reproductions of cathode geometries, arising from their manufacturing simulations, and characterized by different proportions of active material (nickel manganese cobalt - NMC111), and by different calendering degrees [39]. Then, a workflow reproducing the manufacturing process of the electrodes based on coarse-grained molecular dynamics simulations and discrete element method is employed to create the electrode microstructures [40,41]. We compare the classical and autoregressive training strategies to show the best approach to obtain transient predictions.

We present the governing equations as well as the computational details of the electrochemical simulations, the dataset employed for the training of the neural networks, and an overview on multiscale convolutional neural networks. Finally, the generalization capability of the trained MSNet on the prediction of discharge curves for new batteries is presented in the results section.

2. Microstructurally resolved electrochemical model

Electrodes can be modelled as porous media made by two solid phases immersed in the electrolyte. The first solid phase is the active material (AM), which takes part into the electrochemical reaction, the second solid phase is made by the carbon, which ensures electrical conduction throughout the electrode, and the binder, that binds the components together into a stable microstructure. The active material (granulometry ~1–10 μm characteristic size of AM particles) constitutes a phase easily distinguishable from the carbon (~50–150 nm) and the binder components, which instead for modeling purposes are represented by a single phase called carbon binder domain (CBD) [13].

In this work a dataset made by microscale simulations of half-cells (cathode side) has been employed for the training of machine learning models. In this section the transport equations numerically solved to this end are summarized. The equations of mass transport and charge balance must be solved in three domains: AM, CBD, and electrolyte.

In the electrolyte the charge conservation reads as follows:

$$\nabla \cdot i_l = 0, \tag{1.1}$$

$$i_l = -\sigma_l \nabla \phi_l + \frac{2RT\sigma_l}{F}(1-t_+)\left(1+\frac{\partial(\ln f_\pm)}{\partial(\ln c_l)}\right)\nabla \ln(c_l), \tag{1.2}$$

where i_l is the ionic flux in the electrolyte, σ_l is the electrical conductivity of the electrolyte, ϕ_l is the electric potential in the electrolyte, F is the Faraday constant, R is the perfect gas constant, t_+ is the transport number of the lithium ions, $f_\pm$ is the mean molar activity coefficient, c_l is the lithium ions concentration in the electrolyte.

The first term is the charge conservation equation, where $\nabla \cdot i_l$ is null because of the cell neutrality. The current density is made by two terms: the migration contribution, that depends on the electrical conductivity of the electrolyte, and the diffusion contribution that depends on the concentration gradient related to the diffusion coefficient of the ions by the transfer number. The activity coefficient considers the interactions between ions in the solution, in fact, the concentration of the ions is not compatible with a dilute approach, thus the concentrated solution theory applies [42].

The transport equation for the concentration of lithium ions within the electrolyte can be expressed as:

$$\frac{\partial c_l}{\partial t} + \nabla \cdot \left(-\mathscr{D}_l \nabla c_l + \frac{i_l t_+}{F} \right) = 0. \tag{2}$$

In the AM portion of the electrode the charge conservation equation is Ohm's law in steady state conditions:

$$\nabla\cdot\left(\sigma_{s,AM}\nabla\phi_s\right)=0, \tag{3}$$

where $\sigma_{s,AM}$ is the electrical conductivity of AM, and ϕ_s is the potential of the AM.

The mass balance inside the electrode can be modelled by Fick's law, which describes the diffusion of lithium in the AM electrode:

$$\frac{\partial c_s}{\partial t}+\nabla\cdot\left(\mathscr{D}_s\nabla c_s\right)=0, \tag{4}$$

where c_s is the lithium concentration in the AM and $\mathscr{D}_s$ is the diffusion coefficient of lithium.

The CBD is modeled as a homogeneous porous medium domain, so the transport equations are solved in the domain without considering its geometrical internal structure and by assuming the electrolyte fully infiltrating it. The transport properties are averaged over the entire domain, so the charge transport is modelled as follows:

$$\nabla\cdot\left(\sigma_{s,CBD}\nabla\phi_s\right)=0, \tag{5}$$

where $\sigma_{s,CBD}$ is the electrical conductivity of the CBD and is expressed as a function of its porosity.

The mass balance in the CBD is:

$$\frac{\partial\varepsilon_{CBD}c_l}{\partial t}+\nabla\cdot\left(-\mathscr{D}_{l,eff}\nabla c_l+\frac{i_l t_+}{F}\right)=0, \tag{6.1}$$

$$i_l=-\sigma_{l,eff}\nabla\phi_l+\frac{2RT\sigma_{l,eff}}{F}(1-t_+)\left(1+\frac{\partial(\ln f_\pm)}{\partial(\ln c_l)}\right)\nabla\ln(c_l), \tag{6.2}$$

where $\sigma_{l,eff}$ and $\mathscr{D}_{l,eff}$ are the effective electrical conductivity and lithium ions diffusivity in the CBD.

They are defined as a fraction f of the electrolyte properties:

$$\mathscr{D}_{l,eff}=f\,\mathscr{D}_l,\quad \sigma_{l,eff}=f\,\sigma_l. \tag{7}$$

The electrochemical reaction is modeled at the interface by means of the Butler-Volmer equation:

$$i_{se}=Fkc_l^{\alpha_a}c_s^{\alpha_c}\left(c_s^{max}-c_s\right)^{\alpha_c}\left[\exp\left(\frac{\alpha_a F\eta}{RT}\right)-\exp\left(-\frac{\alpha_c F\eta}{RT}\right)\right] \tag{8}$$

where k is the reaction rate coefficient, α_a and α_c are the anodic and cathodic transfer coefficients, and η is the overpotential which is defined as:

$$\eta=\phi_s-\phi_l-E_{eq}, \tag{9}$$

where E_{eq} is the electrode equilibrium potential. On the surface of Li metal which is the reference electrode, an extra contribution is added:

$$\eta=\phi_s-\phi_l-R_{SEI}i-E_{eq}$$

where R_{SEI} is the surface resistence due to solid electrolyte interface (SEI).

3. Dataset

The dataset employed for training the data-driven model was created using half-cell microscale simulations of the cathode side, whose geometries are reproduced in-silico. The physics-based digital twin workflow for the creation of the electrode structures mirrors the experimental steps of electrode manufacturing, as shown in Fig. 1A (more details can be found in [39]). The key steps of the fabrication process digitally reproduced are: (1) the preparation of the slurry with all the components, (2) the slurry casting on the current collector, (3) the solvent evaporation from the cast, (4) the calendering of the dried electrode. The resulting geometry is used to generate the computational grid employed for the electrochemical simulation.

These geometries usually distinguish the solid in two regions: AM and CBD. The latter is constituted by the binder and the conductive carbon, which forms a single phase after the evaporation of the solvent. The in-silico reproduction of the electrode geometry (arising from manufacturing simulations) is preferred over direct imaging in the context of electrochemical simulations. This is because even though 3D images can be obtained using synchrotron X-ray tomographies [43], the segmentation of the three phases (AM, CBD, electrolyte) is not straightforward and is a topic of active research [44]. Being able to create new electrode geometries spanning a wide range of different formulations is essential to create large simulation datasets.

To this end the processes at points (2), (3), (4), are modelled by using the molecular dynamics code LAMMPS [45], as detailed in [39,46]. First, given the granulometry of the AM and of the CBD before the evaporation, a random configuration of particles is produced. Then, the

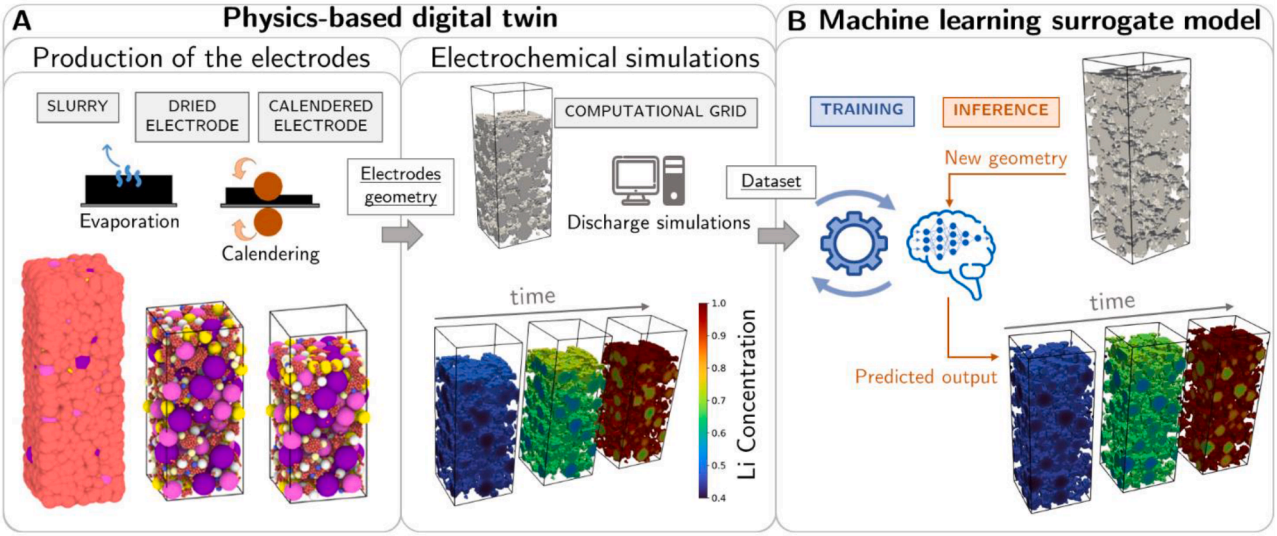

Fig. 1. (A) The physics-based digital twin process replicates the experimental production of electrodes which are then used in the electrochemical simulations to create a dataset. The digital twin results are then used to train the machine learning surrogate model (B) for the prediction of new 3D time-changing fields in new geometries.

slurry is equilibrated at constant pressure and temperature imposing Lennard-Jones and Granular Hertzian potentials between particles. After that, the evaporation of the solvent is modelled imposing the shrinkage of the CBD particles until a set value is reached. Finally, the calendering of the electrode is simulated imposing a compression on the dried virtual electrode. The computational details of this workflow can be found in other previous publications, see for instance [15,39,41,46].

The electrochemical simulations have been performed by using the finite element method implemented in COMSOL. In particular, the partial differential equations of charge and mass balance reported in the previous section are solved in the AM, CBD, and electrolyte phases. The values of the parameters in Eqs. (4)–(12) are reported in Table 1.

The starting point for building the dataset used for the training of the neural networks is choosing a set of different electrode geometries, varying in terms of AM/CBD proportions and calendering degree. Each geometry is then employed for simulations at different discharge rates, i.e., the C rate. These values are also summarized in Table 2; all the possible combinations of those parameters have been simulated to create the dataset, thus a total of 27 transient simulations. The dataset was previously validated by experimental results. Thus, the approach presented in this work does not need further validation and can be considered a self-consistent defined workflow.

Since the simulations have been solved by a finite element method, the computational grids are unstructured. This is not a compatible input for a convolutional neural network, which requires a matricial data shape, so the results have been interpolated into a structured grid, in order to be conveyed to the network as a 3D image. The interpolation consists, at first, in the creation of the Cartesian grid by means of a voxelization algorithm, in the grid '1' is assigned to the phase to be interpolated and '0' elsewhere. Then the fields are interpolated from the unstructured grid to the structured one by means of a Gaussian kernel interpolator [47]. The size of the Cartesian grid cells is 0.5 μm, which is the resolution of the elements in the original unstructured grid [39].

The dataset is made by 27 samples which are defined for a transient problem as the collection of all the timeframes available from a simulation of a given electrode geometry and undergoing a certain discharge rate, so its dimensions are: (time, x, y, z). The time required for a discharge cycle depends on the C rate: if the C rate is doubled, the time required to completely discharge the battery is halved. In the dataset the timeframes have been saved according to the C rate, thus resulting in samples with the same number of timeframes. It is important to underline that the timeframes are not saved at each time-step of the transient simulation, because the memory load necessary to save them would have been prohibitory. 25 timeframes are then available for each sample, for 2C discharge the time interval between two timeframes is 50 s, for 1C discharge rate 100 s, for 0.5C discharge rate 200 s. While the range of discharge rates (C-rates) explorable with this methodology is larger, the chosen C-rates stand in the middle of the significant range for practical battery cell operation relevance. The number of timeframes employed for each simulation is an hyperparameter for the data-driven model, in the case of this work 25 timeframes is a good tradeoff between an accurate description of the discharge dynamics, the computational cost of the training procedure, and the hardware constraints on the GPU. In this work we will refer to the timeframes as a multiple of Δt^*.

The number of timeframes, to extract from the simulations and employ in the training, is surely a hyperparameter to be further investigated to evaluate its impact on the accuracy of the predictions.

Table 2
Parameters explored for the creation of the dataset.

Parameter	Set
AM (%wt)	85–90–95
Calendering degree	0–10–20
C rate	0.5C-1C-2C

4. Machine learning architecture

4.1. Convolutional neural networks

Convolutional neural networks are deep learning models that work with images. In the context of this work, we utilize 3D voxelized domains as inputs.

The basic layer of these models is the convolutional layer which performs the convolution operation ($*$):

$$x_{out} = f\left(\sum_{i=1}^{F} x_{in} * k_i + b_i\right) \tag{10}$$

where f is a pixel-wise non-linear function, x_{in} is the input 3D image, k_i is the kernel, F is the total number of kernels, b_i is a bias term, x_{out} is the 3D output of the operation. The kernel is a 3D operator whose parameters are optimized during the training procedure; for an accurate overview of these operations the reader is referred to [54]. CNN are equivariant to translation, so the network learns how to detect geometric features across the domain, which is fundamental when dealing with porous structures.

Some examples of widely used CNN architectures are U-Net [55] and Res-Net [55]. However, when dealing with 3D images the memory requirements are large, making the use of these standard architectures

Table 1
Parameters of the charge and mass balance equations.

Parameter	Value/Reference
Porosity of CBD ε_{CBD}	0.27 [48]
Maximum Li concentration of NMC c_s^{max} (mol/m^3)	48,207
Initial degree of lithiation (DOL) of NMC	0.45925
Reaction rate coefficient of NMC k (m$^{2.5}$/(s mol$^{0.5}$))	4.38 10^{-11} [49–51]
Reference concentration c_{ref} (mol/m^3)	1000
Ionic conductivity of electrolyte σ_l (S/m)	$0.04(c_l/c_{ref})^5 - 0.4071(c_l/c_{ref})^4 + 1.7131(c_l/c_{ref})^3 - 3.6247(c_l/c_{ref})^2 + 3.3222(c_l/c_{ref}) + 0.016$ [52] at 20 °C
Electrical conductivity of NMC $\sigma_{s,AM}$ (S/m)	0.01
Electrical conductivity of CBD $\sigma_{s,CBD}$ (S/cm)	$-173.967\epsilon + 0.1593$
Deformation of the CBD phase because of calendering ϵ	[37] Table S3
Factor for effective transport correction in CBD f	0.05
Diffusion coefficient of Li$^+$ $\mathscr{D}_l$ m^2/s	$-6e-12(c_l/c_{ref})^3 + 6e-11(c_l/c_{ref})^2 - 3e-10(c_l/c_{ref}) + 5e-10$ [52] at 20 °C
Diffusion coefficient of Li in NMC $\mathscr{D}_s$ m^2/s	$1e-14(c_l/c_{ref})^3 + 3e-14(c_l/c_{ref})^2 - 1e-13(c_l/c_{ref}) + 6e-14$ [53]
Transport number of Li$^+$ t_+	$0.0015(c_l/c_{ref})^3 + 0.0434(c_l/c_{ref})^2 - 0.287(c_l/c_{ref}) + 0.5222$ [52] at 20 °C
Activity dependence of Li$^+$ $\left(1 + \frac{\partial(\ln f_\pm)}{\partial(\ln C_l)}\right)$	$0.1138(c_l/c_{ref})^3 + 0.0944(c_l/c_{ref})^2 + 0.6692(c_l/c_{ref}) + 0.1778$ [52] at 20 °C
Anodic transfer coefficient α_a	0.5
Cathodic transfer coefficient α_c	0.5
SEI film resistance R_{SEI} Ω m^2	0.001

unfeasible. It is possible to overcome this limitation by reducing the size of the images or optimizing the architectural design. Reducing the size of the input images size can be an issue when studying porous media structures since most of the applications need representative elementary volumes as computational domains. Multiscale neural networks (MSNet) have been demonstrated to be an excellent alternative to the previous architectures since its design allows it to process bigger images with a fixed number of trainable parameters [35] compared to the above-mentioned architectures [33].

For this application, we have verified this by building a PoreFlowNet [33] model, which merges the most effective features of both U-Nets and Res-Nets. We have chosen the same number of parameters as the MSNet that we eventually have used for the final training process (i.e.: approximately three million). The higher memory efficiency of MSNet was immediately proven as it was possible to fit only three frames of the time-series in this PoreFlowNet, out of the 25 composing the full transient evolution of the phenomenon.

4.2. Autoregressive MSNet

MSNet is composed by several branches (scales) which are fully convolutional neural networks, each branch gets the same set of input features at different resolution thanks to coarsening operations, then each branch predicts the output field at the corresponding resolution and contributes to the final prediction thanks to refinement operations, the MSNet architecture is shown in Fig. 2.

The process of reducing the resolution of both input and output fields, known as coarsening, is achieved via nearest neighbor averaging. This means that the collective value of every set of 2^3 pixels is averaged and then depicted as one pixel. Conversely, the refinement operation employs a masked nearest-neighbors re-scaling. This method works to retain the geometric form of the solid part. The operations of coarsening and refinement are designed to preserve the spatial average, consequently, when a refined image undergoes coarsening, it reverts to its initial state. The study of the images at different resolutions makes MSNet capable of grasping short-range and long-range correlations in multiscale three-dimensional phenomena. For transient problems, more appropriate architectures and training strategies must be chosen. Recurrent neural networks, such as long-short term memory networks [56], have been widely employed in data science, but may not be the most appropriate structure for a Markovian problem.

In this work MSNet has been modified in order to deal with a transient dataset, and to predict a sequence of fields starting from the initial conditions. The most intuitive way to approach this problem is to consider the problem as a Markovian process: the result at a certain time-step depends just on the previous one, as it is in the solution of a transient physics-based simulation. Therefore, the network should take as input the geometrical descriptors and the operating conditions, together with a temporal feature, which is: the initial condition for the prediction of the first timeframe, or the previous timeframe for the prediction of the following ones.

Given this premise the easiest solution to perform the training is to concatenate the input features with the previous timeframe field (the true field from the simulations) and train the network as the standard MSNet. This is what will be called the "classic" approach. In this way the training is carried out on shuffled timeframes, so the transient problem is decomposed as single frame samples. Nevertheless, for testing purposes the first prediction is carried on concatenating the input features with the initial condition, then the first output is concatenated with the other features for the prediction of the second timeframe, so on and so forth until the last prediction. This is necessary since in the test mode the intermediate timeframes are not available, thus the network predictions have to be employed as input for the following timeframes.

Another training solution is to mimic the testing process, so that during the training the input features are concatenated with the previous timeframe network prediction, and not the true field of the physics-

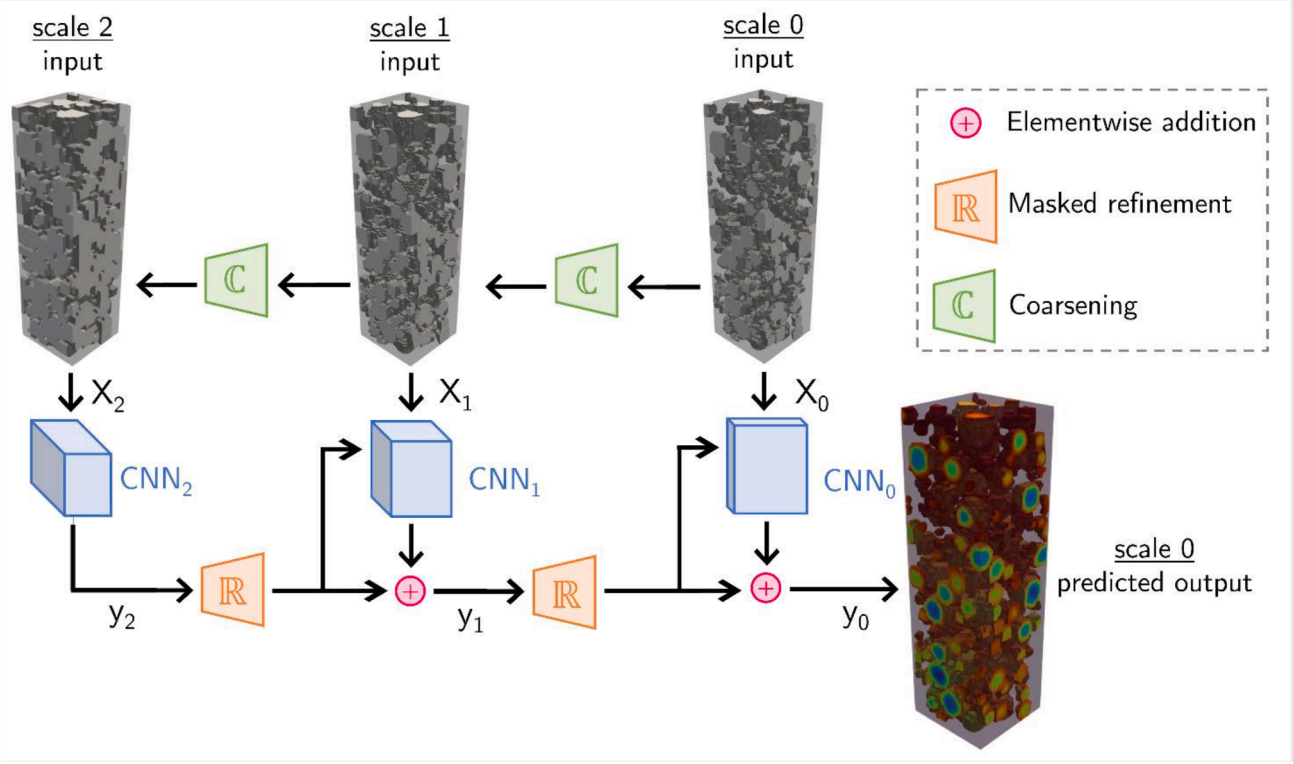

Fig. 2. Workflow of the MSNet architecture. Each scale takes as input the same set of features, at different resolutions, thanks to coarsening operations (only the binary geometry feature is shown). The convolutional layers (blue blocks) have an increasing number of filters for increasing scales to optimize the tradeoff between the total number of trainable parameters and the memory requirements during training.

based simulation. By using this approach, the transient nature of the dataset is preserved, since MSNet is provided with the samples (each one with the timeframes from the initial condition to the final timeframe) at each epoch. This autoregressive training approach, shown in Fig. 3, can be summarized as follows:

$$\hat{y}_{(0,1)} = \mathrm{MSNet}(X_0, X_{\mathrm{initial}}), \tag{11}$$

$$\hat{y}_{(0,2)} = \mathrm{MSNet}\left(X_0, \hat{y}_{(0,1)}\right), \tag{12}$$

$$\hat{y}_{(0,T)} = \mathrm{MSNet}\left(X_0, \hat{y}_{(0,t-1)}\right), \tag{13}$$

where $\hat{y}_{(0,T)}$ is the predicted output at scale 0 and for the last timeframe T, X_0 is the set of input features. For a generic timeframe t, MSNet performs the following operations:

$$\hat{y}_{(0,t)} = CNN_0\left(X_0, \hat{y}_{(0,t-1)}, \mathbb{R}\left(\hat{y}_{(1,t)}\right)\right) + \mathbb{R}\left(\hat{y}_{(1,t)}\right), \tag{14}$$

$$\hat{y}_{(1,t)} = CNN_1\left(X_1, \hat{y}_{(1,t-1)}, \mathbb{R}\left(\hat{y}_{(2,t)}\right)\right) + \mathbb{R}\left(\hat{y}_{(2,t)}\right), \tag{15}$$

$$\hat{y}_{(2,t)} = CNN_2\left(X_2, \hat{y}_{(2,t-1)}\right), \tag{16}$$

where $\mathbb{R}()$ is the refinement operation, CNN_N is the fully convolutional neural network for scale N.

In this work we have trained a 3-scale MSNet (indices from 0 to 2). This was done to ensure a good field of vision [35] for our samples size which is (72,72,244).

The loss function of a single timeframe, $\mathscr{L}_t$, is calculated as the sum of the mean squared errors for each scale (N), the global loss function (minimized during training) is the sum of the loss functions of the single timeframes normalized by the number of timeframes:

$$\mathscr{L}_t = \sum_{N=0}^{2}\left(y_{(N,t)} - \hat{y}_{(N,t)}\right)^2, \tag{17}$$

$$\mathscr{L} = \frac{1}{T}\sum_{t=0}^{T}\mathscr{L}_t, \tag{18}$$

The input features to the network, X_0, are geometrical descriptors and operating conditions. The Euclidean distance transform, the AM-CBD-electrolyte repartition, and the distance between current collector and separator have been employed as geometry features, respectively A, B, C of Fig. 4. In particular the feature A represents the solid phase diffusion distance: in fact it has been employed as an effective feature in informing the network about the characteristic length of a transport diffusion process [36]. Feature C is useful to give information about the directionality of the charge and mass transport processes, happening between the collector and the separator. The C rate value has been provided as operating condition input. Both input and output features have been scaled in order to range between 0 and 1, so MSNet predicts normalized concentration and potential fields.

The architecture details and the training parameters are summarized in Table 3.

5. Results and discussion

The main prediction objective of this study is the reconstruction of the discharge curves, which describe the potential decay as a function of the degree of lithiation of the cathode. So MSNet was employed for the prediction of the lithium concentration field in the AM phase, and the potential field in the solid phase (AM + CBD) of the electrode. From these predicted fields it is possible to integrate their quantities over the phases and obtain the desired discharge curves. First the two training approaches proposed in the previous section are compared for the prediction of the concentration field, then the best approach among the two is employed for the prediction of the potential field, required for the reproduction of the discharge curves.

The comparison is based on the prediction of the lithium concentration on three test samples: with C rates 0.5C, 1C, 2C, all with AM weight percentage equal to 90 and calendering degree equal to 10. In general the choice of the training strategy (in the sense of its impact on the statistical significance of the resulting trained model) is very important, and on a dataset with such a limited size even more so. While techniques based on repeated trainings with varying training subsets (such as k-fold cross-validation) serve the purpose of providing a better estimate of the potential performance of the model at generalization tasks, they are in this case quite costly, and as such we have opted for a physical-based heuristic procedure in which, as mentioned above, the samples sharing the same geometry would be kept out from the training, so to have the network perform its testing on three samples differing from the training set in their most important (read, most defining) feature: the geometry of the computational domain, thus providing for a reasonably testing ground for comparing the classic and autoregressive approach even in generalization.

In the first approach the training inputs are the geometrical descriptors, the C rate, and the previous timeframe field (from the physics-based simulation). In the second approach the training inputs are the geometrical descriptors, the C rate, and the previous network-predicted timeframe field. In Fig. 5 the relative error between true and predicted average lithium concentration is reported for the different C rates along subsequent timeframes. It is evident that by using the first approach the error increases with time, while this does not happen with the second

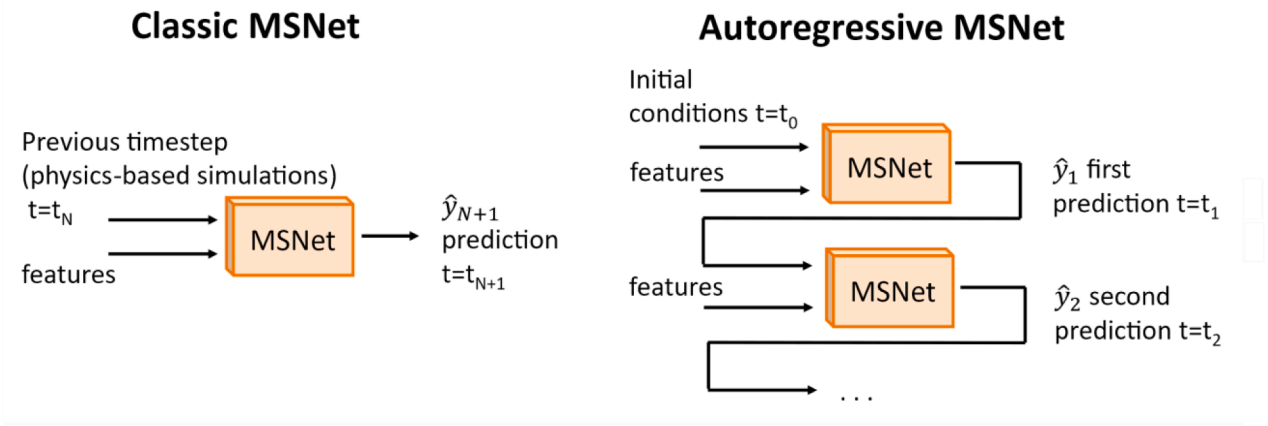

Fig. 3. Classic and autoregressive approaches for the training of MSNet for the prediction of time-dependent fields.

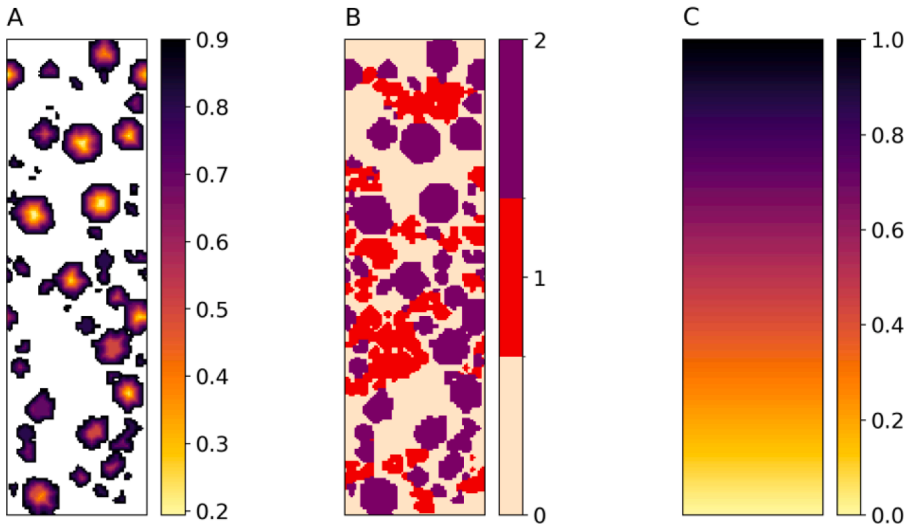

Fig. 4. Geometrical descriptors employed as input to MSNet (cathode: 85% AM, calendering: 0). Plot A: inverted Euclidean distance, plot B: AM/CBD/electrolyte repartition, C: current collector separator distance.

Table 3
Architecture details and chosen hyperparameters.

Parameter	Value
Number of scales (N)	3
Number of convolutional layers per scale	5
Number of filters (F) at the finest scale (0)	10
Number of filters (F) at scale n	10^{4n+1}
Kernel size of the convolutional layers	(3,3,3)
Learning rate	10^{-4}
Batch size	1
Activation function	CELU [57]
Training/test split	24/3
Input size (x,y,z)	(72,72,244)

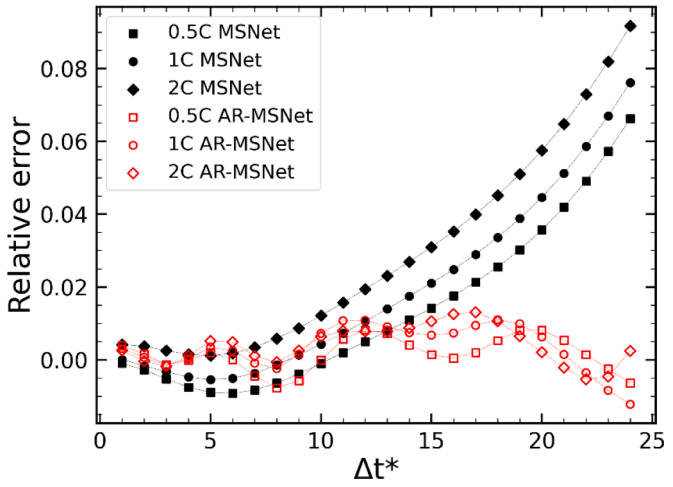

Fig. 5. Error on the prediction of the average concentration along the timeframes and the different C rates. Classic (MSNet in red) and autoregressive (AR-MSNet in black) approaches are compared; squares: 0.5C, circles: 1C, diamonds: 2C.

approach. In Fig. 6 three timeframes for the test sample at discharge 1C are compared for the two approaches. For each timeframe, the true (from the finite elements simulations) and predicted local concentration fields are displayed for a slice of the 3D domain, and the pixel-wise error is reported on the right. It is possible to see that using a "classical" (not autoregressive) approach even the local prediction deteriorates in time, in fact, the radial profile of the lithium concentration is lost in time becoming a random noisy concentration field.

The different behavior in generalization is due to the error propagation in time. When MSNet is trained with the true fields as input, the network is not trained to deal with slight (but cumulating) fluctuations of prediction errors as input fields, thus it is not trained to dampen these fluctuations, on the contrary it magnifies the errors in the predictions leading to a big propagation of the error. In the second approach, during the training the network learns how to dampen fluctuations in the input resulting in much better generalization.

Given these results, the autoregressive MSNet was employed for the prediction of the transient concentration and potential fields. The predictions of the potential fields over time are summarized in Fig. 7 for each timeframe: there, the true field from the COMSOL simulations is reported, then the predicted field, and the local relative error. The average quantities are needed to obtain the predicted discharge curves of Fig. 8. In these charts the potential is expressed as a function of the lithium concentration in the active material for the different C rates. In order to give a more intuitive representation of the evolution in time of these quantities and how the autoregressive MSNet predictions compare to the simulations ground truth, a video is provided with this paper, in the form of Supplementary Material.

6. Conclusions

In this work we have decided to focus on a single, but central, aspect of the field of computer-aided battery research: the problem of facilitating the optimization processes needed in the design of battery electrodes and cells. In the fast-moving landscape of modern battery design, with its demand for ever growing performance in multiple application domains, this means computational loads that workflows based on traditional modeling cannot bear. A wide variety of low-order, data-driven, and in general surrogate models are thus being studied and employed to aid in this prospect.

Our tools of choice for this effort are neural networks, and especially convolutional neural networks. The effectiveness of this kind of machine learning technique is apparent (and was again shown here) when dealing with the interpretation of transport phenomena which are influenced by the geometric structure characterizing the system, as is the case for porous media in general and clearly for heterogeneous microstructure of lithium-ion battery electrodes.

Starting from an innovative multi-scale convolutional network architecture, proven to accurately reproduce results of detailed steady-

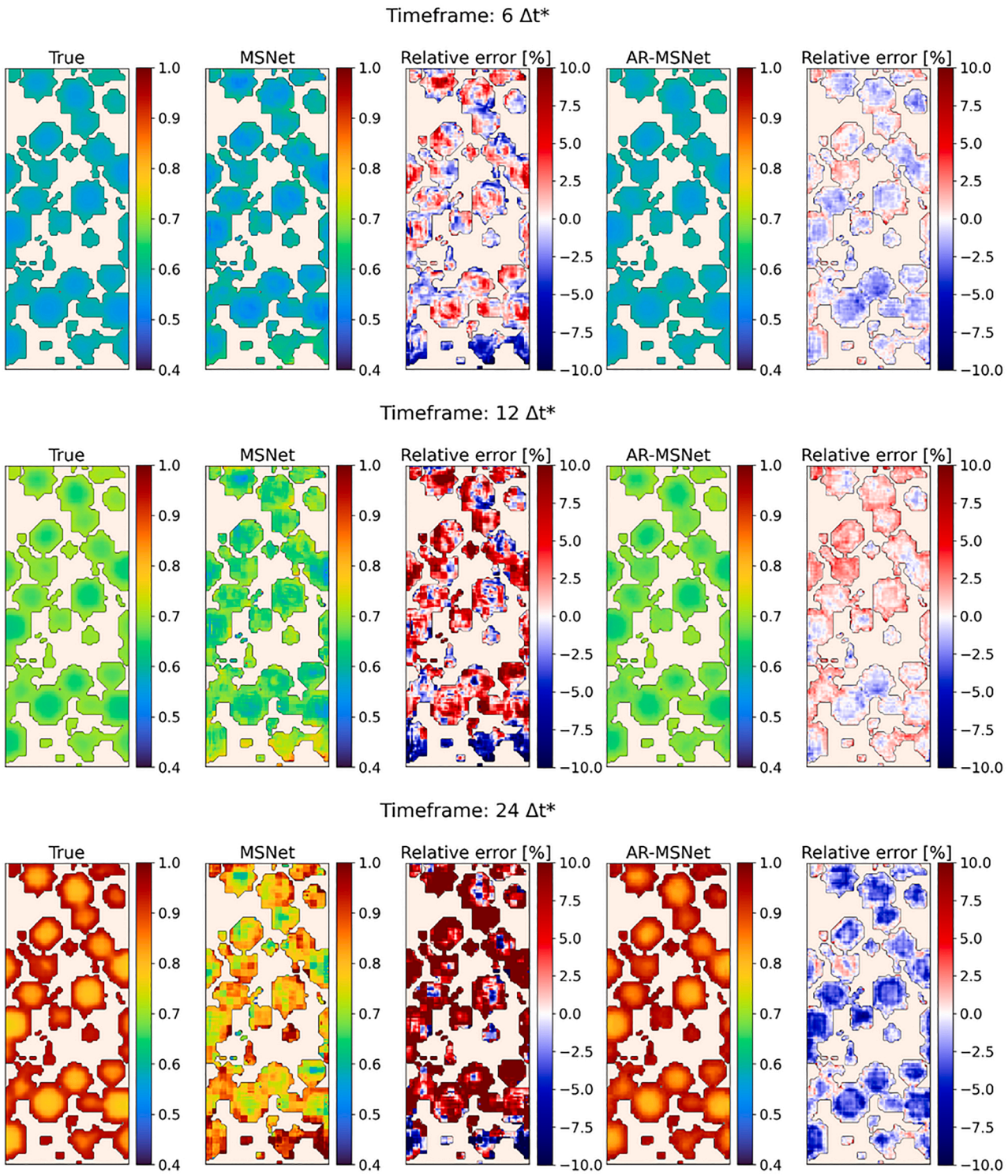

Fig. 6. Local true and predicted concentration fields for three timeframes of a slice of the 3D sample (1C). For each timeframe: concentration field from the physics-based simulation, prediction by the classical MSNet, relative error between true and classical approach, prediction by the autoregressive MSNet, relative error between true and autoregressive MSNet.

state physics-based simulations, we have developed an improvement to obtain a data-driven model able to also explore variations in time and in space of properties of interest.

Two connected takeaways result from the work shown here. First, as mentioned, the results confirm the great flexibility of convolutional neural networks as algorithms for the treatment of physics-based simulation data, and that they are able (with appropriate modifications) to also be effectively used to treat time-varying sequences of three-dimensional data. This was not granted, as this kind of application lies outside of the applications for which convolutional neural networks are now solidly a standard, namely image analysis. Secondly, the process we presented shows how this extension is not trivial, as a "classic" sequential approach to the neural network training would fail by means of error accumulation in time. Thus, an

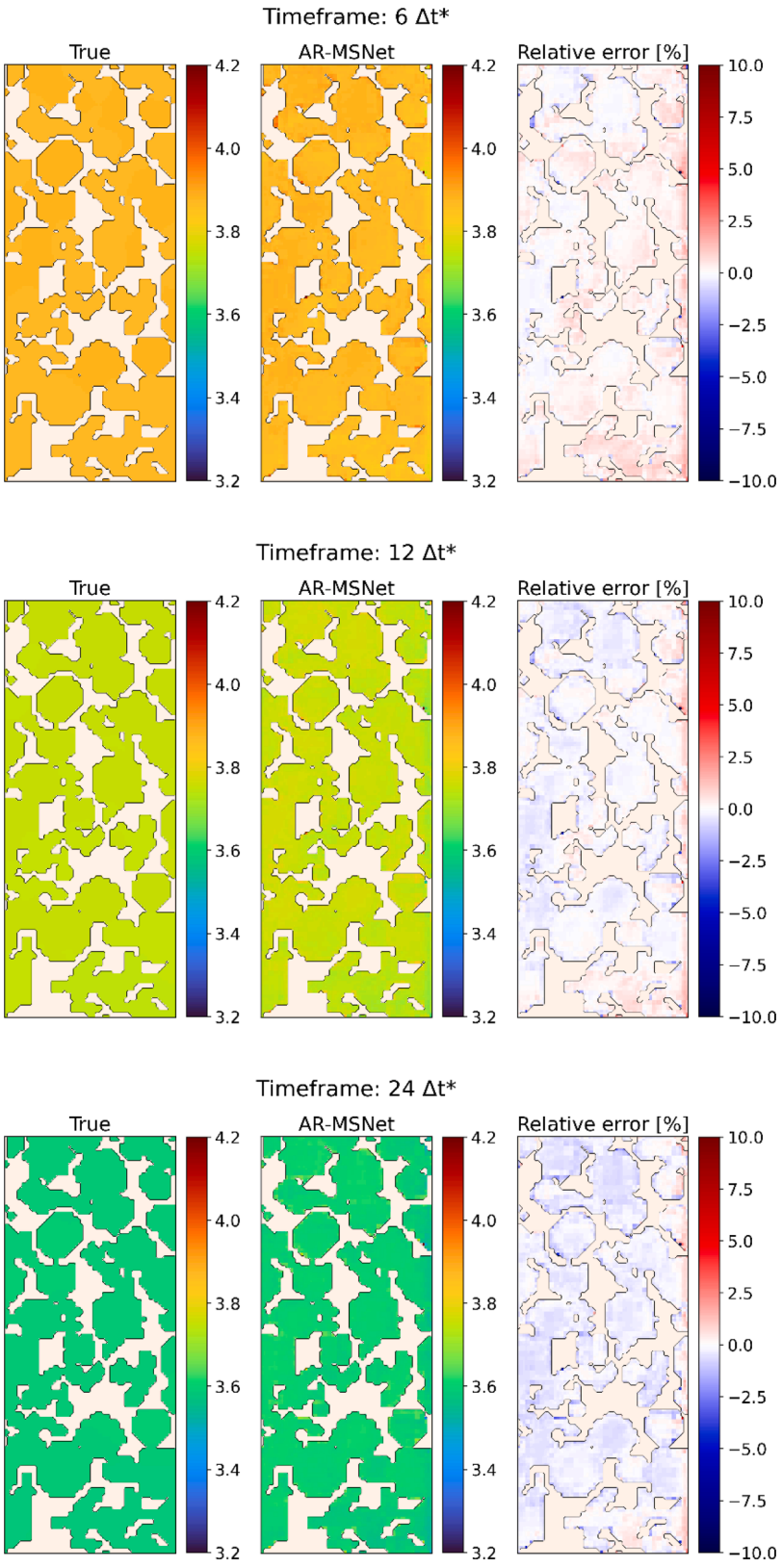

Fig. 7. Local true and predicted potential fields for three timeframes of a slice of the 3D sample (1C). For each timeframe: concentration field from the physics-based simulation, prediction by the autoregressive MSNet, relative error between true and autoregressive MSNet.

autoregressive approach was needed, meaning that both a suitable architecture had to be developed and appropriate loss functions were formulated in order to properly teach the network how to interpret the data coming from physics-based simulations, and how to learn to make comparably good predictions, even when moving beyond the cases on which it was trained.

Being this work a proof-of-concept of the applicability of this approach, there is significant room for improvement. The dataset

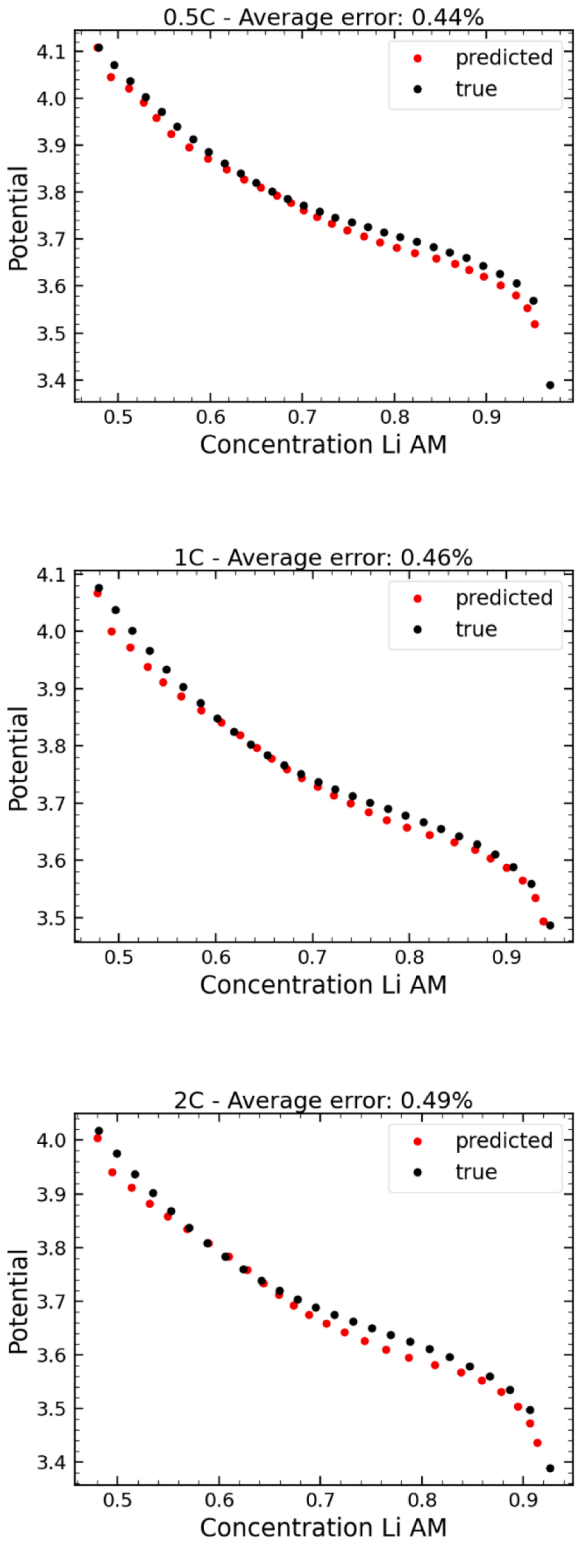

Fig. 8. Discharge curves showing potential versus concentration values for C rates equal to 2C, 1C, 0.5C. True values from simulations compared with predictions by AR-MSNet.

employed for this work is limited to NMC cathodes of Lithium-ion batteries, this means that the trained network cannot generalize to different materials and cells. In the future developments of this work it would be interesting to train the network on a diverse dataset of cells and materials, and test the inference capabilities of the method in predicting the discharge behavior of a wider set of cells and materials.

In conclusion, we consider this to be a successful proof of concept for fast, reliable, and full-order surrogation of accurate numerical simulations. Fast surrogate models are essential to deal with the wide parameter space intrinsic in contemporary battery design and optimization [24]: the results of this work aim to show how such surrogates can not only predict single key metrics but are also able to disclose the full dynamics of battery systems as they evolve in time.

The major opportunity of the approach we propose is that we pave the way towards computational high-throughput screening of 3D-resolved heterogeneous electrode operation as a function of manufacturing parameters, and therefore towards computational optimization of the electrodes [24].

CRediT authorship contribution statement

Agnese Marcato: Conceptualization, Methodology, Software, Validation, Formal analysis, Investigation, Writing – original draft. **Javier E. Santos:** Conceptualization, Methodology, Software, Writing – review & editing. **Chaoyue Liu:** Conceptualization, Methodology, Software, Validation, Formal analysis, Investigation, Data curation, Writing – original draft. **Gianluca Boccardo:** Conceptualization, Supervision, Writing – review & editing, Funding acquisition. **Daniele Marchisio:** Conceptualization, Supervision, Writing – review & editing, Funding acquisition. **Alejandro A. Franco:** Conceptualization, Methodology, Supervision, Writing – review & editing, Resources, Project administration, Funding acquisition.

Declaration of Competing Interest

The authors declare that they have no known competing financial interests or personal relationships that could have appeared to influence the work reported in this paper.

Acknowledgments

The authors acknowledge the large-scale European research initiative Battery 2030+ (under grant agreement No. 957213) and the Battery Interface Genome – Materials Acceleration Platform project (www.big-map.eu, under grant agreement No. 957189). Computational resources provided by hpc@polito, which is a project of Academic Computing within the Department of Control and Computer Engineering at the Politecnico di Torino (www.hpc.polito.it); we also acknowledge the CINECA award under the ISCRA initiative (IsC96_NTPM-II), for the availability of high-performance computing resources and support. A.A. F. and C.L. acknowledge the European Union's Horizon 2020 research and innovation program for the funding support through the European Research Council (grant agreement No. 772873, "ARTISTIC" project). A. A.F. acknowledges Institut Universitaire de France for the support. A.M. and J.E.S gratefully acknowledge the support of the U.S. Department of Energy through the LANL/LDRD Program and the Center for Non-Linear Studies.

Supplementary materials

Supplementary material associated with this article can be found, in the online version, at doi:10.1016/j.ensm.2023.102927.

References

[1] A. Fotouhi, D.J. Auger, K. Propp, S. Longo, M. Wild, A review on electric vehicle battery modelling: from Lithium-ion toward Lithium–Sulphur, Renew. Sustain. Energy Rev. 56 (2016) 1008–1021, https://doi.org/10.1016/j.rser.2015.12.009.
[2] M. Astaneh, D. Maggiolo, H. Ström, Finite-size effects on heat and mass transfer in porous electrodes, Int. J. Therm. Sci. 179 (2022), 107610, https://doi.org/10.1016/j.ijthermalsci.2022.107610.
[3] A.A. Franco, A. Rucci, D. Brandell, C. Frayret, M. Gaberscek, P. Jankowski, P. Johansson, Boosting rechargeable batteries R&D by multiscale modeling: myth

or reality? Chem. Rev. 119 (2019) 4569–4627, https://doi.org/10.1021/acs.chemrev.8b00239.
[4] Z. Deng, V. Kumar, F.T. Bölle, F. Caro, A.A. Franco, I.E. Castelli, P. Canepa, Z. W. Seh, Towards autonomous high-throughput multiscale modelling of battery interfaces, Energy Environ. Sci. 15 (2022) 579–594, https://doi.org/10.1039/D1EE02324A.
[5] D. Dessantis, P. Di Prima, D. Versaci, J. Amici, C. Francia, S. Bodoardo, M. Santarelli, Aging of a lithium-metal/LFP cell: predictive model and experimental validation, Batteries 9 (2023) 146, https://doi.org/10.3390/batteries9030146.
[6] A. Jokar, B. Rajabloo, M. Désilets, M. Lacroix, Review of simplified Pseudo-two-Dimensional models of lithium-ion batteries, J. Power Sources 327 (2016) 44–55, https://doi.org/10.1016/j.jpowsour.2016.07.036.
[7] M. Lagnoni, C. Nicolella, A. Bertei, Survey and sensitivity analysis of critical parameters in lithium-ion battery thermo-electrochemical modeling, Electrochim. Acta 394 (2021), 139098, https://doi.org/10.1016/j.electacta.2021.139098.
[8] V. Sulzer, S.G. Marquis, R. Timms, M. Robinson, S.J. Chapman, Python battery mathematical modelling (PyBaMM), J. Open Res. Softw. 9 (2021) 14, https://doi.org/10.5334/jors.309.
[9] M. Doyle, T.F. Fuller, J. Newman, Modeling of galvanostatic charge and discharge of the lithium/polymer/insertion cell, J. Electrochem. Soc. 140 (1993) 1526, https://doi.org/10.1149/1.2221597.
[10] X. Lu, A. Bertei, D.P. Finegan, C. Tan, S.R. Daemi, J.S. Weaving, K.B. O'Regan, T.M. M. Heenan, G. Hinds, E. Kendrick, D.J.L. Brett, P.R. Shearing, 3D microstructure design of lithium-ion battery electrodes assisted by X-ray nano-computed tomography and modelling, Nat. Commun. 11 (2020) 2079, https://doi.org/10.1038/s41467-020-15811-x.
[11] M.M. Forouzan, C.W. Chao, D. Bustamante, B.A. Mazzeo, D.R. Wheeler, Experiment and simulation of the fabrication process of lithium-ion battery cathodes for determining microstructure and mechanical properties, J. Power Sources 312 (2016) 172–183, https://doi.org/10.1016/j.jpowsour.2016.02.014.
[12] M. Chouchane, A.A. Franco, About the consideration of the inactive materials and the meshing procedures in computational models of lithium ion battery electrodes, ChemElectroChem 9 (2022), e202200692, https://doi.org/10.1002/celc.202200692.
[13] A.C. Ngandjong, A. Rucci, M. Maiza, G. Shukla, J. Vazquez-Arenas, A.A. Franco, Multiscale simulation platform linking lithium ion battery electrode fabrication process with performance at the cell level, J. Phys. Chem. Lett. 8 (2017) 5966–5972, https://doi.org/10.1021/acs.jpclett.7b02647.
[14] J. Scharf, M. Chouchane, D.P. Finegan, B. Lu, C. Redquest, M. Kim, W. Yao, A. A. Franco, D. Gostovic, Z. Liu, M. Riccio, F. Zelenka, J.M. Doux, Y.S. Meng, Bridging nano- and microscale X-ray tomography for battery research by leveraging artificial intelligence, Nat. Nanotechnol. 17 (2022) 446–459, https://doi.org/10.1038/s41565-022-01081-9.
[15] M. Chouchane, A. Rucci, T. Lombardo, A.C. Ngandjong, A.A. Franco, Lithium ion battery electrodes predicted from manufacturing simulations: assessing the impact of the carbon-binder spatial location on the electrochemical performance, J. Power Sources 444 (2019), 227285, https://doi.org/10.1016/j.jpowsour.2019.227285.
[16] V. De Lauri, L. Krumbein, S. Hein, B. Prifling, V. Schmidt, T. Danner, A. Latz, Beneficial effects of three-dimensional structured electrodes for the fast charging of lithium-ion batteries, ACS Appl. Energy Mater. 4 (2021) 13847–13859, https://doi.org/10.1021/acsaem.1c02621.
[17] M. Parmananda, C. Norris, S.A. Roberts, P.P. Mukherjee, Probing the role of multi-scale heterogeneity in graphite electrodes for extreme fast charging, ACS Appl. Mater. Interfaces 14 (2022) 18335–18352, https://doi.org/10.1021/acsami.1c25214.
[18] R. Barnett, F. Municchi, J. King, M. Icardi, Electrochemical transport modelling and open-source simulation of pore-scale solid-liquid systems, (2022). http://arxiv.org/abs/2212.13519 (accessed April 4, 2023).
[19] A. Chauhan, E. Asylbekov, S. Kespe, H. Nirschl, Influence of carbon binder domain on the performance of lithium-ion batteries: impact of size and fractal dimension, Electrochem. Sci. Adv. 3 (2023), e2100151, https://doi.org/10.1002/elsa.202100151.
[20] G.M. Goldin, A.M. Colclasure, A.H. Wiedemann, R.J. Kee, Three-dimensional particle-resolved models of Li-ion batteries to assist the evaluation of empirical parameters in one-dimensional models, Electrochim. Acta 64 (2012) 118–129, https://doi.org/10.1016/j.electacta.2011.12.119.
[21] D. Maggiolo, F. Picano, F. Zanini, S. Carmignato, M. Guarnieri, S. Sasic, H. Ström, Solute transport and reaction in porous electrodes at high Schmidt numbers, J. Fluid Mech. 896 (2020) A13, https://doi.org/10.1017/jfm.2020.344.
[22] A.H. Wiedemann, G.M. Goldin, S.A. Barnett, H. Zhu, R.J. Kee, Effects of three-dimensional cathode microstructure on the performance of lithium-ion battery cathodes, Electrochim. Acta 88 (2013) 580–588, https://doi.org/10.1016/j.electacta.2012.10.104.
[23] Z.A. Khan, M. Agnaou, M.A. Sadeghi, A. Elkamel, J.T. Gostick, Pore network modelling of galvanostatic discharge behaviour of lithium-ion battery cathodes, J. Electrochem. Soc. 168 (2021), 070534, https://doi.org/10.1149/1945-7111/ac120c.
[24] M. Duquesnoy, C. Liu, D.Z. Dominguez, V. Kumar, E. Ayerbe, A.A. Franco, Machine learning-assisted multi-objective optimization of battery manufacturing from synthetic data generated by physics-based simulations, Energy Storage Mater. 56 (2023) 50–61, https://doi.org/10.1016/j.ensm.2022.12.040.
[25] N. Di Pasquale, J.D. Elliott, P. Hadjidoukas, P. Carbone, Dynamically polarizable force fields for surface simulations via multi-output classification neural networks, J. Chem. Theory Comput. 17 (2021) 4477–4485, https://doi.org/10.1021/acs.jctc.1c00360.
[26] A. Marcato, D. Marchisio, G. Boccardo, Reconciling deep learning and first-principle modelling for the investigation of transport phenomena in chemical engineering, Can. J. Chem. Eng. (2023), https://doi.org/10.1002/cjce.24838 n/a.
[27] A. Massei, N. Falco, D. Fissore, Use of machine learning tools and NIR spectra to estimate residual moisture in freeze-dried products, Spectrochim. Acta A Mol. Biomol. Spectrosc. 293 (2023), 122485, https://doi.org/10.1016/j.saa.2023.122485.
[28] Z. Jiang, J. Li, Y. Yang, L. Mu, C. Wei, X. Yu, P. Pianetta, K. Zhao, P. Cloetens, F. Lin, Y. Liu, Machine-learning-revealed statistics of the particle-carbon/binder detachment in lithium-ion battery cathodes, Nat. Commun. 11 (2020) 2310, https://doi.org/10.1038/s41467-020-16233-5.
[29] Y.D. Wang, M. Shabaninejad, R.T. Armstrong, P. Mostaghimi, Deep neural networks for improving physical accuracy of 2D and 3D multi-mineral segmentation of rock micro-CT images, Appl. Soft Comput. 104 (2021), 107185, https://doi.org/10.1016/j.asoc.2021.107185.
[30] L. Liu, M. Prodanović, M.J. Pyrcz, Impact of geostatistical nonstationarity on convolutional neural network predictions, Comput. Geosci. 27 (2023) 35–44, https://doi.org/10.1007/s10596-022-10181-3.
[31] A. Marcato, G. Boccardo, D. Marchisio, From computational fluid dynamics to structure interpretation via neural networks: an application to flow and transport in porous media, Ind. Eng. Chem. Res 61 (2022) 8530–8541, https://doi.org/10.1021/acs.iecr.1c04760.
[32] R.M. Weber, S. Korneev, I. Battiato, Homogenization-informed convolutional neural networks for estimation of Li-ion battery effective properties, Transp. Porous Media 145 (2022) 527–548, https://doi.org/10.1007/s11242-022-01862-9.
[33] J.E. Santos, D. Xu, H. Jo, C.J. Landry, M. Prodanović, M.J. Pyrcz, PoreFlow-Net: a 3D convolutional neural network to predict fluid flow through porous media, Adv. Water Resour. 138 (2020), 103539, https://doi.org/10.1016/j.advwatres.2020.103539.
[34] A.K. Ting, J.E. Santos, E. Guiltinan, Using machine learning to predict multiphase flow through complex fractures, Energies 15 (2022) 8871, https://doi.org/10.3390/en15238871.
[35] J.E. Santos, Y. Yin, H. Jo, W. Pan, Q. Kang, H.S. Viswanathan, M. Prodanović, M. J. Pyrcz, N. Lubbers, Computationally efficient multiscale neural networks applied to fluid flow in complex 3D porous media, Transp. Porous Media 140 (2021) 241–272, https://doi.org/10.1007/s11242-021-01617-y.
[36] A. Marcato, J.E. Santos, G. Boccardo, H. Viswanathan, D. Marchisio, M. Prodanović, Prediction of local concentration fields in porous media with chemical reaction using a multi scale convolutional neural network, Chem. Eng. J. 455 (2023), 140367, https://doi.org/10.1016/j.cej.2022.140367.
[37] B. Chang, J. Santos, R. Victor, H. Viswanathan, M. Prodanovic, Improving Machine Learning Predictions of Rock Electric Properties using 3D Geometric Features, OnePetro, 2022, https://doi.org/10.2118/210456-MS.
[38] C. Chang, E. Santos, ElRock-Net: assessing the utility of machine learning to initialize 3D electric potential simulations, (2022).
[39] C. Liu, T. Lombardo, J. Xu, A.C. Ngandjong, A.A. Franco, An experimentally-validated 3D electrochemical model revealing electrode manufacturing parameters' effects on battery performance, Energy Storage Mater. 54 (2023) 156–163, https://doi.org/10.1016/j.ensm.2022.10.035.
[40] T. Lombardo, F. Caro, A.C. Ngandjong, J.B. Hoock, M. Duquesnoy, J.C. Delepine, A. Ponchelet, S. Doison, A.A. Franco, The ARTISTIC online calculator: exploring the impact of lithium-ion battery electrode manufacturing parameters interactively through your browser, Batter. Supercaps 5 (2022), e202100324, https://doi.org/10.1002/batt.202100324.
[41] A.C. Ngandjong, T. Lombardo, E.N. Primo, M. Chouchane, A. Shodiev, O. Arcelus, A.A. Franco, Investigating electrode calendering and its impact on electrochemical performance by means of a new discrete element method model: towards a digital twin of Li-Ion battery manufacturing, J. Power Sources 485 (2021), 229320, https://doi.org/10.1016/j.jpowsour.2020.229320.
[42] G.W. Richardson, J.M. Foster, R. Ranom, C.P. Please, A.M. Ramos, Charge transport modelling of Lithium-ion batteries, Eur. J. Appl. Math. 33 (2022) 983–1031, https://doi.org/10.1017/S0956792521000292.
[43] Z. Deng, X. Lin, Z. Huang, J. Meng, Y. Zhong, G. Ma, Y. Zhou, Y. Shen, H. Ding, Y. Huang, Recent progress on advanced imaging techniques for lithium-ion batteries, Adv. Energy Mater. 11 (2021), 2000806, https://doi.org/10.1002/aenm.202000806.
[44] F.L.E. Usseglio-Viretta, A. Colclasure, A.N. Mistry, K.P.Y. Claver, F. Pouraghajan, D.P. Finegan, T.M.M. Heenan, D. Abraham, P.P. Mukherjee, D. Wheeler, P. Shearing, S.J. Cooper, K. Smith, Resolving the discrepancy in tortuosity factor estimation for Li-ion battery electrodes through micro-macro modeling and experiment, J. Electrochem. Soc. 165 (2018) A3403, https://doi.org/10.1149/2.0731814jes.
[45] A.P. Thompson, H.M. Aktulga, R. Berger, D.S. Bolintineanu, W.M. Brown, P. S. Crozier, P.J. in 't Veld, A. Kohlmeyer, S.G. Moore, T.D. Nguyen, R. Shan, M. J. Stevens, J. Tranchida, C. Trott, S.J. Plimpton, LAMMPS - a flexible simulation tool for particle-based materials modeling at the atomic, meso, and continuum scales, Comput. Phys. Commun. 271 (2022), 108171, https://doi.org/10.1016/j.cpc.2021.108171.
[46] A. Rucci, A.C. Ngandjong, E.N. Primo, M. Maiza, A.A. Franco, Tracking variabilities in the simulation of Lithium Ion Battery electrode fabrication and its impact on electrochemical performance, Electrochim. Acta 312 (2019) 168–178, https://doi.org/10.1016/j.electacta.2019.04.110.
[47] U. Ayachit, The ParaView Guide, Guide Books, 2015, https://doi.org/10.5555/2789330.

[48] S.R. Daemi, C. Tan, T. Volkenandt, S.J. Cooper, A. Palacios-Padros, J. Cookson, D.J. L. Brett, P.R. Shearing, Visualizing the carbon binder phase of battery electrodes in three dimensions, ACS Appl. Energy Mater. 1 (2018) 3702–3710, https://doi.org/10.1021/acsaem.8b00501.

[49] J. Sturm, A. Rheinfeld, I. Zilberman, F.B. Spingler, S. Kosch, F. Frie, A. Jossen, Modeling and simulation of inhomogeneities in a 18650 nickel-rich, silicon-graphite lithium-ion cell during fast charging, J. Power Sources 412 (2019) 204–223, https://doi.org/10.1016/j.jpowsour.2018.11.043.

[50] C. Liu, H. Li, X. Kong, J. Zhao, Modeling analysis of the effect of battery design on internal short circuit hazard in LiNi0.8Co0.1Mn0.1O2/SiOx-graphite lithium ion batteries, Int. J. Heat Mass Transf. 153 (2020), 119590, https://doi.org/10.1016/j.ijheatmasstransfer.2020.119590.

[51] J. Smekens, J. Paulsen, W. Yang, N. Omar, J. Deconinck, A. Hubin, J. Van Mierlo, A modified multiphysics model for lithium-ion batteries with a LixNi1/3Mn1/3Co1/3O2 electrode, Electrochim. Acta 174 (2015) 615–624, https://doi.org/10.1016/j.electacta.2015.06.015.

[52] J. Landesfeind, H.A. Gasteiger, Temperature and concentration dependence of the ionic transport properties of lithium-ion battery electrolytes, J. Electrochem. Soc. 166 (2019) A3079, https://doi.org/10.1149/2.0571912jes.

[53] S.L. Wu, W. Zhang, X. Song, A.K. Shukla, G. Liu, V. Battaglia, V. Srinivasan, High rate capability of Li(Ni1/3Mn1/3Co1/3)O2 electrode for Li-ion batteries, J. Electrochem. Soc. 159 (2012) A438, https://doi.org/10.1149/2.062204jes.

[54] I. Goodfellow, Y. Bengio, A. Courville, Deep Learning, MIT Press, 2016.

[55] K. He, X. Zhang, S. Ren, J. Sun, Deep residual learning for image recognition, (2015). 10.48550/arXiv.1512.03385.

[56] F.A. Gers, N.N. Schraudolph, J. Schmidhuber, Learning precise timing with lstm recurrent networks, J. Mach. Learn. Res. 3 (2003) 115–143, https://doi.org/10.1162/153244303768966139.

[57] J.T. Barron, Continuously differentiable exponential linear units, (2017). 10.48550/arXiv.1704.07483.